Three-Dimensional Visualization of Proteins within Metal-Organic Frameworks via Ferritin-Enabled Electron Microscopy

Authors and Affiliations: Rakia Dhaoui[1], Saira L. Cazarez[1], Li Xing[2], Elmira Baghdadi[1], Justin T. Mulvey[3], Nehal S. Idris[1], Paul J. Hurst[1], M. Paula Vena[4], Giuseppe Di Palma[1], Joseph P. Patterson[1,3]

[1] Department of Chemistry, University of California, Irvine, Irvine, California 92697-2025, United States

[2] Irvine Materials Research Institute, University of California, Irvine, Irvine, CA 92697-2025, United States

[3] Department of Materials Science and Engineering, University of California, Irvine, Irvine, CA 92697-2025, United States

[4] Laboratory of Physical Chemistry, Department of Chemical Engineering, Eindhoven University of Technology, Eindhoven, The Netherlands

Keywords: Transmission Electron Tomography, Metal-Organic Frameworks, Encapsulation, Crystallization, Biopolymers

Abstract: Electron tomography holds great promise as a tool for investigating the three-dimensional (3D) morphologies and internal structures of metal-organic framework-based protein biocomposites (protein@MOFs). Understanding the 3D spatial arrangement and density of proteins within protein@MOFs is paramount for developing synthetic methods to control protein spatial distribution within the crystals. In this study, we leverage the naturally occurring iron oxide mineral core of the protein horse spleen ferritin (Fn) as a contrast agent to directly observe individual proteins once encapsulated into MOFs by electron microscopy methods. Our methodology couples scanning electron microscopy, transmission electron microscopy, and electron tomography to garner a detailed 3D structural interpretation of the Fn@MOFs addressing the significant gaps in our understanding of protein spatial localization and aggregation. Our findings collectively reveal that adjusting the ligand-to-metal ratios, protein concentration, and the use of denaturing agents alters how proteins are arranged, localized, and aggregated within MOF crystals.

1. Introduction

Enhancing protein stability and performance through encapsulation into synthetic hosts has led to the development of biocomposite materials, [1–6] with metal-organic frameworks (MOFs) emerging as promising candidates.[7,8] MOFs are porous crystalline materials comprised of metal ions or metal-containing clusters coordinated to polydentate organic linkers to form channels connected in one-, two-, or three-dimensions.[9–11] This modular architecture offers ample design space to tailor biohybrid materials for specific applications in biotechnology and biomedicine.[12–14] A significant challenge in optimizing the synthetic conditions for targeted protein@MOF crystals is the lack of detailed information on protein arrangement, localization, and aggregation at the individual protein level. This limitation hinders the ability to design synthetic methods to control protein@MOF crystallization mechanisms and properties such as catalytic activity, protective capacity, and stability.[8,12,15,16]

The prevailing methods to assess protein spatial distribution in protein@MOFs involve indirect studies conducted after thermal calcination[17,18] or confocal laser scanning microscopy (CLSM) paired with fluorescent protein labeling.[7,15,19–25] Although CLSM is a powerful tool for evaluating the overall protein spatial distribution, its spatial resolution is limited, and protein modifications can impact their localization.[15,26] Transmission electron microscopy (TEM) is a widely employed technique for examining the crystallinity, dynamics, and composition of MOFs with high spatial resolution.[27] However, the electron transparency of proteins encapsulated within MOFs has obstructed the direct observation of individual proteins.[25,28,29] As a result, scanning transmission electron microscopy (STEM) imaging and elemental mapping with energy dispersive X-ray (EDX) spectroscopy have been applied to visualize metalloproteins within MOFs by

detecting the metal-containing active site.[29–33] However, achieving resolution at the level of individual proteins has remained elusive.

Here, we take advantage of the naturally occurring iron oxide mineral core in the protein horse spleen ferritin (Fn) to enable direct visualization of individual proteins in protein@MOF crystals by electron microscopy.[34,35] In a prior work, Chen *et al.* used Fn encapsulated into ZIF-8 (Fn@ZIF-8) to confirm protein encapsulation by TEM for their study on intracellular delivery.[36] Recently, Ouyang *et al.* demonstrated the direct TEM visualization of proteins encapsulated within porous hydrogen-bonded organic frameworks by labeling the proteins with Pt nanoclusters.[37,38] Despite these advances in direct TEM visualization of proteins encapsulated in porous frameworks, the detailed 3D arrangement and distribution of encapsulated proteins in these biohybrid materials have yet to be fully elucidated.

Our approach employs the intrinsic iron oxide mineral core in the protein Fn as a contrast agent for encapsulation into MOFs, allowing for detailed spatial insights into protein distribution by SEM, TEM, and ET. This enabled the assessment and quantification of the 3D protein spatial localization and aggregation within protein@MOF crystals. The next major advances in protein immobilization would be the ability to rationally design hybrid biomaterials for novel, highly controlled platforms capable of enhancing protein stability, performance, and recyclability based on the interfacial structures of the proteins used. Our method demonstrates a powerful strategy toward this goal where we show that protein distribution and aggregation can be tailored through manipulation in the synthetic strategy, laying the groundwork for more efficient advancements in the development of protein-based biohybrid materials.

2. Results

Strategy for Design of Fn@MOF Biocomposites

The Fn@MOFs were synthesized using the biomimetic MOF crystallization approach (**Figure 1**).[7] Under this protein encapsulation approach, proteins with low isoelectric points (pI < 7) have been shown to play a crucial role in inducing MOF formation.[7,12,18] Horse spleen Fn is a globular protein composed of a 12 nm diameter protein shell (apoferritin, AFn) that houses a ~6-8 nm diameter densely-packed hydrated iron oxide mineral core in its cavity.[34,39] Horse spleen Fn was selected among the broad class of ferritin iron storage proteins because of its low isoelectric point (~5.0),[12] known stability to the electron beam,[35] and wide commercial availability. For the encapsulation of Fn, two distinct MOF carriers were selected: zeolitic imidazole framework-8 (ZIF-8) and $Eu_2(1,4\text{-BDC})_3(H_2O)_4$ MOF (Eu-BDC). ZIF-8 was chosen as the primary candidate for ET studies due to its well-demonstrated capability as a protein carrier[12] and established understanding of electron beam-sample interactions.[25,28] Eu-BDC was also selected due to its high atomic number lanthanide metal node, which allowed exploration into the limits of Fn visualization by electron microscopy within MOFs.

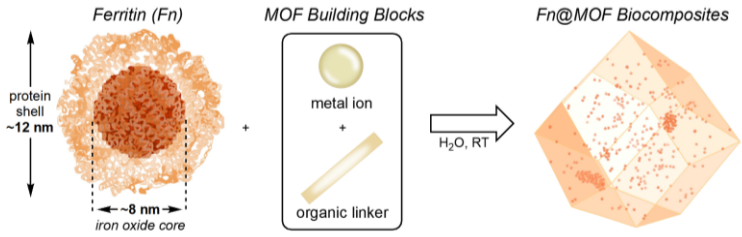

Figure 1. Schematic representation of protein encapsulation via biomimetic MOF crystallization with the protein Fn.

Characterization of Fn@MOF Biocomposites

Research efforts on protein@MOFs have primarily focused on investigating ZIF-8 as the underlying MOF matrix.[12] ZIF-8 is constituted by linking Zn(II) ions with deprotonated 2-methylimidazole (mIm) to form an extended structure of sodalite topology with pore cavities of 3.4 Å.[40] Previous studies of ZIF-8 biocomposites have demonstrated that distinct polymorphs, pseudopolymorphs, and amorphous precursor phases form during biomimetic MOF crystallization.[12] Through manipulation of the synthetic method, different ZIF-based material phases composed of Zn(II) and mIm have been identified outside of ZIF-8, including dia(Zn), ZIF-L, ZIF-C, ZIF-EC1, U12, and amorphous $Zn(mIm)_2$.[15,41–43] Understanding the precise spatial distribution, localization, and aggregation of proteins within these different ZIF-based material phases is crucial for optimizing their properties toward specific applications. To this end, Fn@ZIF-based biocomposites were formed with differing material phases by varying the ligand-to-metal ratio (70:1, 35:1, 17.5:1, 10:1, or 4:1) and Fn protein concentration (0.5 or 2.5 mg/mL).

PXRD analysis was employed to characterize the phase purity and topological identity of the Fn@ZIF-based biocomposites formed at nominally low Fn concentrations **(Figure 2a)**. For the biocomposites formed at ligand-to-metal ratios of 70:1, 35:1, and 17.5:1, the recorded patterns exhibit sharp peaks that show agreement with the simulated pattern for ZIF-8 **(Figure S1)**. For the biocomposites formed at lower ligand-to-metal ratios of 10:1 and 4:1, the recorded patterns show agreement with the simulated patterns for the polymorph dia(Zn) and the pseudopolymorph ZIF-CO_3-1 (ZIF-C) **(Figure S1)**. PXRD analysis was additionally employed for the Fn@ZIF-based biocomposites formed at higher Fn protein concentrations **(Figure S2)**. For ligand-to-metal ratios of 70:1, 35:1, and 17.5:1, the experimental PXRD showed phase-pure ZIF-8 formation. For the lower ligand-to-metal ratios of 10:1 and 4:1, PXRD showed ZIF-C formation with notable amorphous Zn(mIm)$_2$ and ZIF-EC1 formation.[43] Lastly, the PXRD of 1:1 Fn@Eu-BDC (0.5 mg/mL) and 1:1 Eu-BDC **(Figure S3a)** showed the formation of poorly crystalline material matching previous reports.[7,44] Fourier Transform Infrared (FTIR) spectroscopy was next employed to confirm Fn loading **(Figure 2b)**. For the Fn@ZIF-8, Fn@dia(Zn), and Fn@ZIF-C, characteristic proteinaceous amide I and amide II bands were observed centered around 1660 and 1580 cm^{-1}, respectively.[45] Pure ZIF-8 and dia(Zn) are shown in **Figure S4**.

The encapsulation efficiencies of the Fn@MOFs were next assessed to confirm that the biocomposites formed exhibit comparable phase-dependent encapsulation trends as previous reports that use differing protein systems.[26,42] To do so, the differences in the concentration of Fn in the supernatant before and after encapsulation were examined following the linearized Bradford method.[46] As shown in **Figure 2c**, moderate to high encapsulation efficiencies (≥60%) were obtained for all the crystals formed at the differing ligand-to-metal ratios studied with low and high Fn protein concentrations. Notably, the Fn@ZIF-8 formed at higher ligand-to-metal ratios of 70:1 and 35:1 showed lower EE% compared to an intermediate ligand-to-metal ratio of 17.5:1. Additionally, the dia(Zn) polymorph and ZIF-C pseudopolymorph provided much higher protein loadings compared to ZIF-8 (with EE% ≥98%).

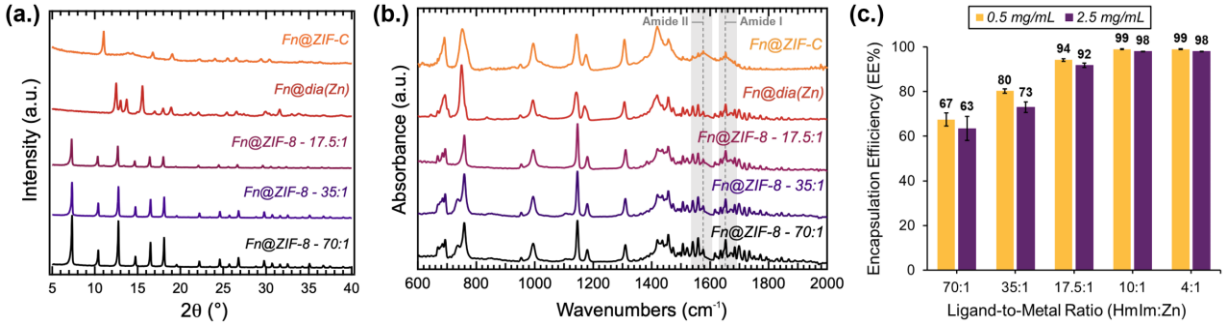

Figure 2. Characterization of Fn@ZIF-based biocomposites. **(a.)** Experimental PXRD patterns of Fn@ZIF-8 (70:1, 35:1, and 17.5:1), 10:1 Fn@dia(Zn), and 4:1 Fn@ZIF-C formed at Fn protein concentrations of 0.5 mg/mL. **(b.)** FTIR spectra for Fn@ZIF-8 (70:1, 35:1, and 17.5:1), 10:1 Fn@dia(Zn), and 4:1 Fn@ZIF-C. Amide I and II bands from Fn are highlighted in grey. **(c.)** Encapsulation efficiencies of Fn@ZIF-based biocomposites formed at varying ligand-to-metal ratios (70:1, 35:1, 17.5:1, 10:1, 4:1) and Fn concentrations (0.5 mg/mL and 2.5 mg/mL). Error bars = Standard Deviation (n = 10).

Direct Observation of Surface-Bound Fn by SEM

Using SEM, surface-bound Fn would be directly visualized due to the increased elastic scattering of the densely packed iron oxide mineral core housed within the hollow protein shell. Inspection of the SEM images on the crystals formed at low protein concentrations revealed high-contrast nanospheres **(Figure 3)**. The nanospheres had average full-width half-max (FWHM) diameters of ~11 nm (**Figure S12f**), interpreted as originating from the iron oxide protein core. Rhombic dodecahedron morphology was observed for the Fn@ZIF-8 formed at ligand-to-metal ratios of 70:1, 35:1, and 17.5:1. For the 10:1 Fn@dia(Zn) crystals, a hexagonal sheet morphology was observed with Fn distribution along the sheets. For the 4:1 Fn@ZIF-C crystals, an irregular twinned granular morphology was observed as the predominant product with Fn on the crystal surfaces. A star-shaped sheet morphology was observed as a minor product with minimal Fn core observed on the surfaces of the crystals (**Figure S7b**). For the Fn@Eu-BDC, an irregular lamellar-bladed morphology was observed with Fn observed on the crystal surfaces. As controls, SEM images were taken of 70:1 ZIF-8 **(Figure 4a)** and 1:1 Eu-BDC **(Figure S3b)**, and neither of the crystals showed the high contrast nanospheres observed for the Fn@MOF crystals. Further confirmation of Fn encapsulation was demonstrated using SEM-EDS, where Fe is observed in the EDS spectra for the biocomposites formed **(Figure S5)**.

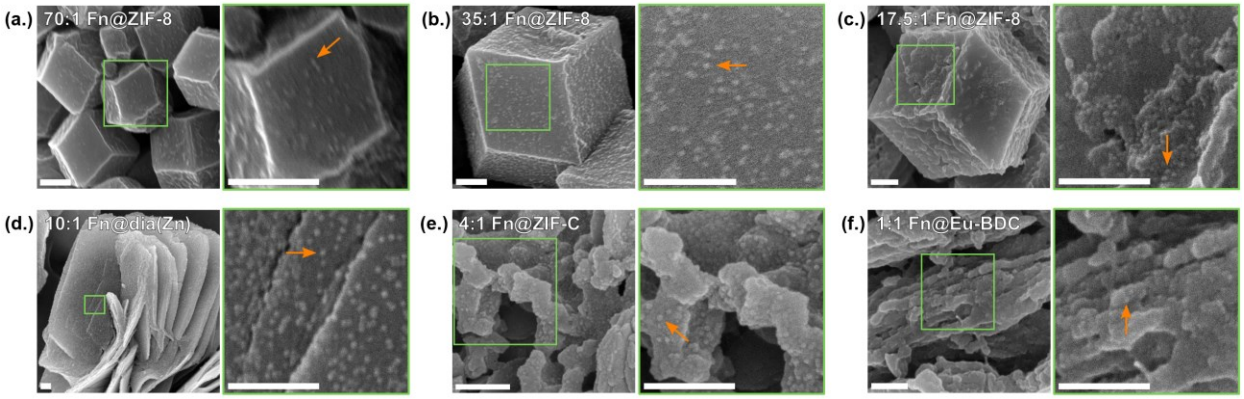

Figure 3. SEM images of **(a.)** 70:1 Fn@ZIF-8, **(b.)** 35:1 Fn@ZIF-8, **(c.)** 17.5:1 Fn@ZIF-8, **(d.)** 10:1 Fn@dia(Zn), **(e.)** 4:1 Fn@ZIF-C, and **(f.)** 1:1 Fn@Eu-BDC formed at Fn concentrations of 0.5 mg/mL. Green boxes indicate regions imaged at higher magnifications. Orange arrows indicate where Fn iron oxide cores are directly visualized. Scale bars are 200 nm.

SEM analysis of the biocomposites formed at high protein concentrations showed high-contrast nanospheres **(Figure S6)**. Rhombic dodecahedron morphology was observed for all the Fn@ZIF-8 samples formed at high Fn concentration, where significant protein density was seen on the crystal surfaces **(Figure 4c, Figure S6a-b)**. A sheet morphology was observed for the 10:1 Fn@ZIF-C crystals, with homogeneous and highly dense Fn observed throughout the surfaces (**Figure S6c**). A spherical morphology was also observed for the 10:1 Fn@ZIF-C synthetic condition as a minor product (**Figure S7a**), attributed to the ZIF-EC1 formed by PXRD.[42,43] For the 4:1 Fn@ZIF-C crystals, a granular morphology with high Fn core density was observed **(Figure S6d)**. Although SEM analysis reveals surface-bound protein, SEM analysis cannot distinguish whether the proteins are surface-adsorbed or surface-localized.

More rigorous evaluations of protein@MOFs utilize the surfactant sodium dodecyl sulfate (SDS) to remove surface-adsorbed protein.[53] The utility of this method was assessed on the 70:1 Fn@ZIF-8 biocomposites with Fn protein concentrations of 0 (control), 0.5, and 2.5 mg/mL **(Figure 4)**. Sodalite topology is conserved for all the SDS-washed Fn@ZIF-8 crystals **(Figure S8a)**. After post-synthetic washing of the 70:1 ZIF-8 and Fn@ZIF-8 crystals with SDS, the edges of the {110} facets show signs of disassembly with a noticeable reduction in Fn core density observed for the biocomposites. Additional SEM-EDS was conducted on the 70:1 Fn@ZIF-8 crystals washed with SDS **(Figure S8b)**, where the spectra showed diminished Fe, providing further evidence of protein removal. To understand whether the surfactant wash with SDS removed only surface-adsorbed proteins, the biocomposites were further analyzed by TEM. The TEM images of 70:1 Fn@ZIF-8 (2.5 mg/mL) with and without SDS washing **(Figure 5a, Figure S9)** revealed the removal of surface-adsorbed and encapsulated surface-localized proteins, as well as signs of MOF support degradation. This constitutes the first direct evidence of surfactant removal of surface-encapsulated proteins in protein@MOFs crystals. This direct visualization of Fn in Fn@MOFs enables control over surface-adsorbed protein contribution and prevent encapsulated protein removal.

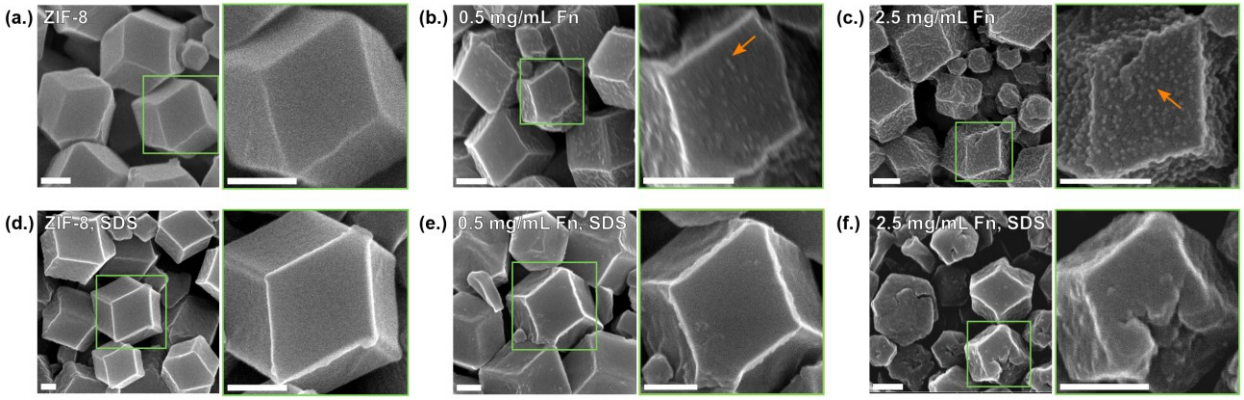

Figure 4. SEM images of **(a.)** 70:1 ZIF-8, **(b.)** 70:1 Fn@ZIF-8 (0.5 mg/mL), **(c.)** 70:1 Fn@ZIF-8 (2.5 mg/mL), **(d.)** 70:1 ZIF-8 (post-SDS wash), **(e.)** 70:1 Fn@ZIF-8 (0.5 mg/mL, post-SDS wash), **(f.)** 70:1 Fn@ZIF-8 (2.5 mg/mL, post-SDS wash). Green boxes indicate regions imaged at higher magnifications. Orange arrows indicate where Fn iron oxide cores are visualized. Scale bars are 200 nm.

Direct Observation of Fn Localization by Dry-CryoTEM

Previous studies on MOFs have noted electron beam damage effects at nanometer length scales due to knock-on damage, local heating, and radiolysis, which limits the resolution achievable in electron microscopy and tomography experiments.[48–53] Dry-cryogenic electron microscopy and tomography techniques (dry-cryoEM and dry-cryoET) were employed to overcome this challenge.[54,55] Surface-localized protein was observed for the Fn@ZIF-8 crystals formed at low Fn concentrations **(Figure 5a-c)**. As the ligand-to-metal ratio decreased, increased aggregation and surface-localized density of the Fn iron oxide cores was observed. For Fn@dia(Zn) and Fn@ZIF-C crystals, compact and evenly distributed Fn protein cores were observed **(Figure 5d-e)**. Lastly, the Fn@Eu-BDC crystals had uniformly distributed Fn cores in the lamellar sheets **(Figure 5f)**. Dry-cryoTEM preparation allowed us to observe minor phases **(Figure S10)**. For the 35:1 Fn@ZIF-8 synthetic condition, sheets with minimal Fn core incorporation and amorphous material with high Fn core density were observed. For the 17.5:1 Fn@ZIF-8, minor crystals formed with significant macropores. Finally, for the 4:1 Fn@ZIF-C, a star-shaped morphology was observed with low Fn density.

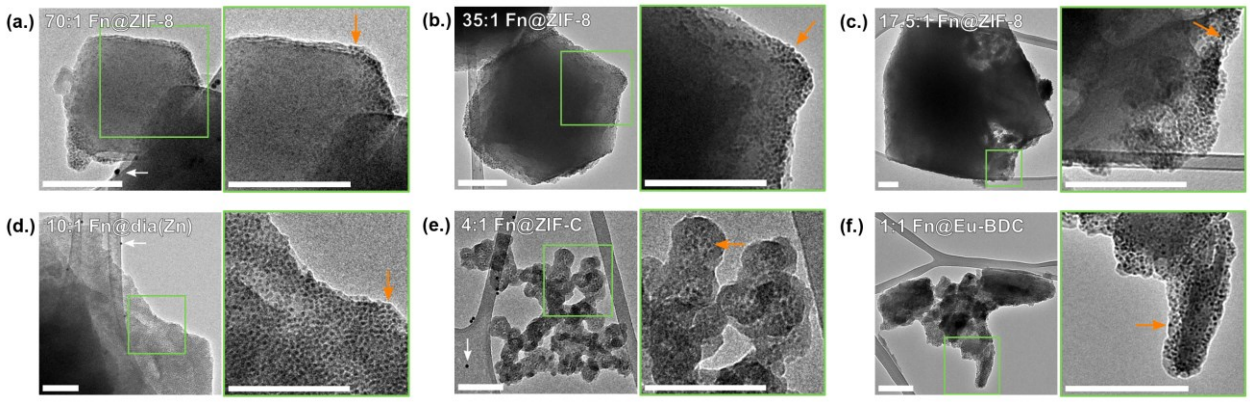

Figure 5. Dry-cryoTEM images of **(a.)** 70:1 Fn@ZIF-8, **(b.)** 35:1 Fn@ZIF-8, **(c.)** 17.5:1 Fn@ZIF-8, **(d.)** 10:1 Fn@dia(Zn), **(e.)** 4:1 Fn@ZIF-C, and **(f.)** 1:1 Fn@Eu-BDC formed at Fn concentrations of 0.5 mg/mL. Green boxes indicate regions imaged at higher magnifications. Orange arrows indicate where Fn iron oxide cores are visualized. White arrows indicate 15 nm gold fiducial markers. The scale bars are 200 nm.

The differing spatial localizations and distribution patterns observed for the Fn@ZIF-based biocomposites prompted us to explore their pH-triggered release profiles (**Figure S11**). A major requirement for protein delivery systems is the efficient release of the encapsulated protein cargos after internalization under physiologically acidic conditions.[36,56] We examined the time-dependent release profiles of Fn at pH 5.5 conditions to understand how each different material phase releases protein cargo. For all the biocomposites formed at low protein concentrations, the Fn@ZIF-C showed the highest rate of dissolution with 100% of the Fn released after 90 min. An intermediate dissolution rate was observed for the 10:1 Fn@dia(Zn) biocomposite, with 78% of Fn released after 180 min. The slowest rates of dissolution were observed for the 70:1 and 35:1 Fn@ZIF-8 biocomposites, with only ~60% Fn release after 180 min. Notably, the 17.5:1 Fn@ZIF-8 sample had much faster dissolution compared to the other Fn@ZIF-8 biocomposites, where 100% dissolution was observed after 150 min. In combination with our direct TEM visualization of the Fn protein cores, we show that lower ligand-to-metal ratios produce $Zn(mIm)_2$ crystalline material phases (e.g., Fn@dia(Zn) and Fn@ZIF-C) with spatially uniform protein densities compared to the higher ratios, which resulted in Fn@ZIF-8 crystals with surface-localized protein. Of these $Zn(mIm)_2$ material phases, Fn@dia(Zn) provides much higher stability under acidic conditions compared to Fn@ZIF-C. For the Fn@ZIF-8 biocomposites, much higher stability is conferred to the crystals formed under high ligand-to-metal ratios of 70:1 and 35:1 compared to the intermediate ratio of 17.5:1. We attribute this difference the observed pores throughout the crystals in the 17.5:1 Fn@ZIF-8, where the defective MOF crystals leads to lower acid stability compared to the crystals with higher crystallinity.[25,42]

To determine the size distribution of the Fn iron oxide core, vitreous cryoTEM samples of neat Fn were prepared **(Figure 6a)**. The cryoTEM images of Fn revealed high-contrast nanospheres with average FWHM diameters of ~7 nm **(Figure S12d)**. Analysis of the Fn iron oxide cores in the TEM images of the 70:1 Fn@ZIF-8 crystals displayed a similar size distribution to the neat Fn **(Figure S12e)**. Both neat Fn and Fn@ZIF-8 crystals exhibited variations in core sizes due to differences in Fe content.[34,39] The TEM images of the analogous surface-adsorbed 70:1 Fn-on-ZIF-8 displayed surface-attached protein, with the entire iron oxide core observable over the ZIF-8 crystals **(Figure 6b)**. The nanospheres in the SEM and TEM images were validated using small-angle X-ray scattering (SAXS) **(Figure 6c)**. The SAXS data for 70:1

Fn@ZIF-8 (2.5 mg/mL) exhibited a broad peak at q-values between 0.06 and 0.1 A^{-1} (~9 nm) absent in the 70:1 ZIF-8 control, indicating the presence of nanostructures within the Fn@ZIF-8 crystals attributed to the Fn core. Furthermore, the biocomposites of horse spleen apoferritin (aFn) were formed, which lacks the iron oxide mineral core.[39] By PXRD, the peaks in the formed 70:1 aFn@ZIF-8 (2.5 mg/mL) crystals matched the simulated pattern for ZIF-8 **(Figure S13)**. The TEM images of the aFn@ZIF-8 crystals revealed surface-localized mesopores, approximately 8-20 nm in size, with no observation of high-contrast nanospheres (**Figure 6d**). These mesopores were attributed to the hollow spherical core, approximately 8 nm in diameter for aFn.[34] Without visualization of the Fn core in the Fn@ZIF-8 crystals, it would be challenging to confidently conclude that the pores come from the hollow aFn cavity. The SEM images of the aFn@ZIF-8 crystals did not show high-contrast nanospheres, in contrast to the Fn@ZIF-8 crystals (**Figure 6e**). Additional SEM-EDS analysis confirmed the absence of Fe in the aFn@ZIF-8 biocomposite, providing further evidence of the lack of an iron oxide core in the aFn@ZIF-8 crystals (**Figure 6f**).

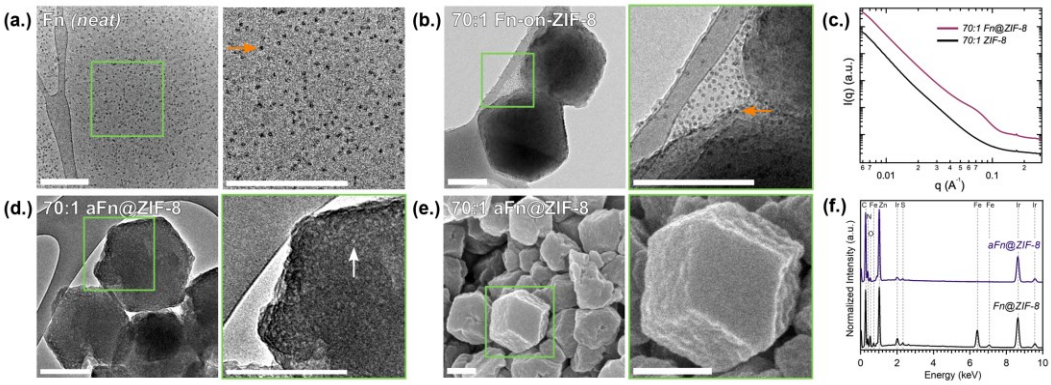

Figure 6. (a.) CryoTEM image of neat Fn. **(b.)** TEM image of 70:1 Fn-on-ZIF-8 (2.5 mg/mL). **(c.)** SAXS patterns of ZIF-8 *(bottom)* and 70:1 Fn@ZIF-8 (2.5 mg/mL) *(top)*. **(d.)** TEM image of 70:1 aFn@ZIF-8 (2.5 mg/mL). **(e.)** SEM image of 70:1 aFn@ZIF-8 (2.5 mg/mL). **(f.)** Experimental EDS spectra of 70:1 Fn@ZIF-8 *(bottom)* and 70:1 aFn@ZIF-8 *(top)*. Green boxes indicate regions imaged at higher magnifications. White arrows indicate areas where surface mesopores are observed. Orange arrows indicate where Fn iron oxide cores are visualized. Scale bars are 200 nm.

3D Visualization of Fn Distribution by Dry-CryoET

While conventional TEM provides 2D images of specimens, ET provides 3D data and allows for cross-sectional data reconstructions, enabling more profound insights into the internal structures of the specimens. To minimize structural damage and mass loss caused by radiolysis, cryogenic-temperature ET was employed.[48,51,52,57] Dry-cryogenic preparation was used to obtain better signal-to-noise images than conventional solvated cryoTEM.[54,55] The dry-cryoET experiments were performed on 70:1 Fn@ZIF-8 crystals formed at low and high protein concentrations, as they produced the smallest and most size-homogeneous Fn@ZIF-8 crystals ideal for ET. **Figure 7** and **Movies S1 and S6** show representative cross-sections of the crystals. These cross-sections reveal surface-localized and surface-bound Fn on both rhombic dodecahedron crystals formed at low and high protein concentrations. Significant observation of partially exposed surface-localized Fn is observed in both crystals **(Figure 9a, c)**.

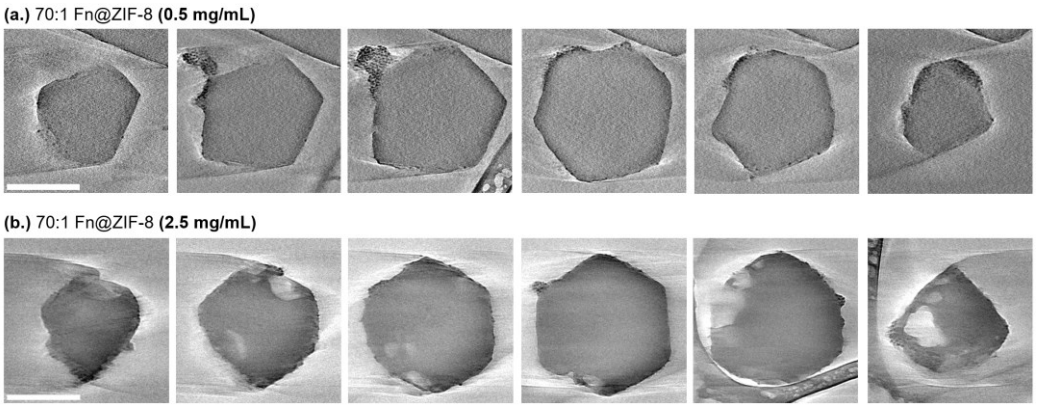

Figure 7. Representative cross sections of **(a.)** 70:1 Fn@ZIF-8 (0.5 mg/mL) and **(b.)** 70:1 Fn@ZIF-8 (2.5 mg/mL) from dry-cryoET. Scale bars are 200 nm.

Noticeable Fn aggregation was observed on the surface of the crystal formed at lower protein concentrations in the 3D volume representations **(Figure 8a-b, Movie S2)**. The Fn aggregates observed outside the MOF crystal are attributed to surface-adsorbed protein or surface-attachment of amorphous $Zn(mIm)_2$ phases with high Fn density. The crystal formed at higher protein concentrations exhibits more uniformly surface-localized Fn aggregates and areas with significant macropores. These macroporous regions with reduced Fn localization are evident in the 3D volume representation and the TEM image of the crystal formed at high Fn concentrations **(Figure 8c-d, Movie S7)**.

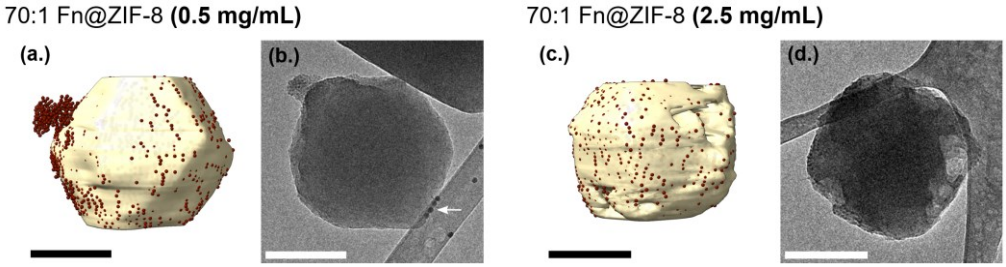

Figure 8. 3D volume representation of the reconstructed **(a.)** 70:1 Fn@ZIF-8 (0.5 mg/mL) and **(c.)** 70:1 Fn@ZIF-8 (2.5 mg/mL). Dry-state cryoTEM images of crystals chosen for dry-cryoET: **(b.)** 70:1 Fn@ZIF-8 (0.5 mg/mL) and **(d.)** 70:1 Fn@ZIF-8 (2.5 mg/mL) with exposure times for image acquisition of 0.3 s. Scale bars are 200 nm.

An aggregate of Fn@ZIF-8 crystals formed at low protein concentrations was also assessed by dry-cryoET **(Figure 9b, Movie S5)**. TEM images and representative cross-sections of the aggregate of crystals are shown in **Figure S14**. Analysis of the 8 MOF crystals confirmed surface-localized protein and aggregation on and between ZIF-8 crystals. Notably, smaller crystals (<100 nm) exhibited uniformly distributed Fn throughout the MOF crystal **(Figure 9bi)**. Mesopores were observed in the larger crystallites (~200 nm), where precise Fn localization is observed **(Figure 9cii)**.

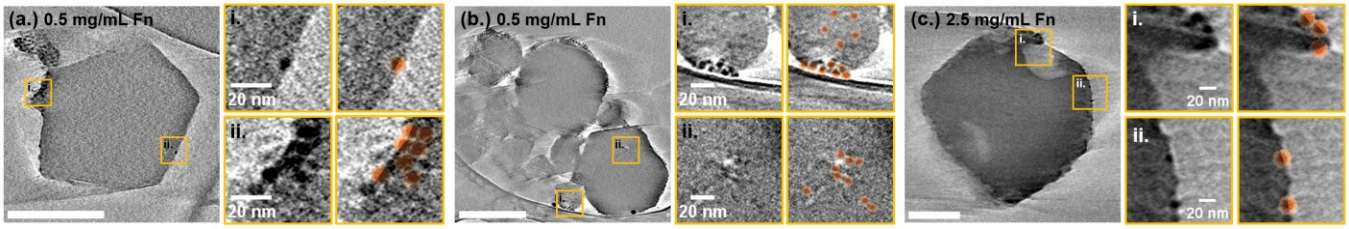

Figure 9. Analysis of cross-sections for the **(a.)** 70:1 Fn@ZIF-8 (0.5 mg/mL) crystal, **(b.)** aggregate of 70:1 Fn@ZIF-8 (0.5 mg/mL) crystals, and **(c.)** 70:1 Fn@ZIF-8 (2.5 mg/mL) crystal. Yellow boxes indicate regions of interest with overlaid cartoons of Fn protein structures. Scale bars are 200 nm unless otherwise noted.

Dry-cryoET was attempted on the 10:1 Fn@dia(Zn) and 4:1 Fn@ZIF-C crystals formed at low protein concentrations to explore their protein spatial distribution and extent of aggregation. However, these different Fn@ZIF-based material phases demonstrated much greater beam sensitivity in comparison to Fn@ZIF-8 crystals, which would require more sensitive detectors or optimized imaging conditions for comprehensive ET analysis. Instead, the spatial distribution of proteins in the Fn@dia(Zn) and Fn@ZIF-C crystals was analyzed using limited tilts (-30, 0, and +30°). As illustrated in **Figure S15**, both Fn@dia(Zn) and Fn@ZIF-C crystals displayed homogeneous spatial distribution where the Fn core was observed throughout the crystals with substantial protein aggregation.

The ET data enabled the quantification of protein spatial location and aggregation **(Figure 10)**. Here, an in-house Matlab script was developed to classify protein location in the protein@MOF crystals as external, surface, or internal based on the relative location of the Fn cores to the MOF crystal surface. The Fn cores are defined as external when the core centers are distances > 6 nm outside the MOF crystal surface, surface-bound if within < 6 nm relative to the MOF crystal surface, and internal if > 6 nm inside the MOF crystal surface (details in SI). By this definition, surface-bound proteins have some portion of the protein residing under the crystal surface and, therefore, partially trapped within the MOF crystal lattice. In contrast, external and internal proteins are fully exposed or encapsulated. The ferritin spatial location analysis **(Figure 10a, c)** reveals that most of the encapsulated Fn in both 70:1 Fn@ZIF-8 crystals, irrespective of protein concentration during synthesis, are surface-exposed (>60%). The 70:1 Fn@ZIF-8 crystal formed at high Fn concentrations has slightly more internal Fn, while the one formed at lower Fn concentrations has significantly more external Fn.

Protein aggregation was next assessed by qualifying the clustering of the Fn cores. A cluster is defined as a group of Fn cores with a center-to-center Fn core distance of ≤ 12.5 nm. Clusters with no adjacent Fn are defined as isolated (details in SI). The ferritin aggregation analysis **(Figure 10b, d)** reveals significantly more aggregation (determined by clustering size) in the 70:1 Fn@ZIF-8 (0.5 mg/mL) crystal and higher amounts of small clusters (size ranges < 11) in 70:1 Fn@ZIF-8 (2.5 mg/mL) crystal.

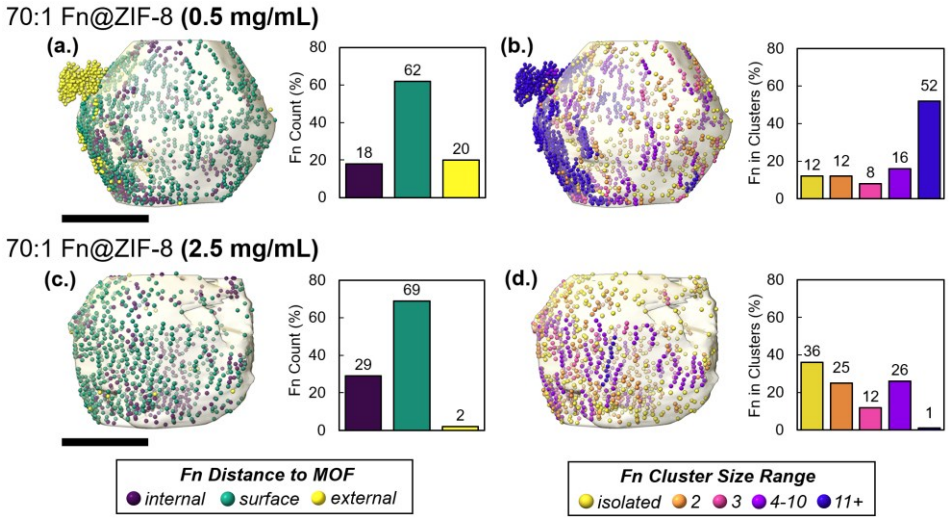

Figure 10. 3D volume representation of dry-cryoET reconstruction showing the Fn core spatial location and MOF crystal surface for the **(a.)** 70:1 Fn@ZIF-8 (0.5 mg/mL) and **(c.)** 70:1 Fn@ZIF-8 (2.5 mg/mL) crystals. Internal Fn (purple spheres) distances are > 6 nm outside of the MOF crystal surface, surface Fn (teal spheres) distances are < 6 nm relative to the MOF crystal surface, and internal Fn (yellow spheres) distances are > 6 nm inside of the MOF crystal. 3D volume representation of dry-cryoET reconstruction showing the Fn core aggregation and MOF crystal surface for the **(b.)** 70:1 Fn@ZIF-8 (0.5 mg/mL) and **(d.)** 70:1 Fn@ZIF-8 (2.5 mg/mL). Isolated Fn cores are represented as dark yellow spheres, clusters of 2 as orange spheres, clusters of 3 as pink spheres, clusters consisting of 4-10 proteins as purple spheres, and clusters of 11+ proteins as blue spheres. The 70:1 Fn@ZIF-8 (0.5 mg/mL) reconstruction contained 1573 segmented Fn cores, and the 70:1 Fn@ZIF-8 (2.5 mg/mL) reconstruction contained 843 segmented Fn cores. Scale bars are 200 nm.

3. Discussion

In recent years, a new paradigm has emerged for understanding how proteins impact the crystallization of metal-organic frameworks.[58] Our group contributed toward this effort by using lattice-resolution cryoTEM to study the nucleation and growth of ZIF-8 crystals in the presence of the protein bovine serum albumin (BSA).[28] Subsequent work by Wu *et al.* used cryoET and molecular simulation to explore mesopore formation that arose from encapsulating glucose oxidase (GOx) in ZIF-8 and an amorphous ZIF-8 precursor phase.[22] Recent work by Tong *et al.* investigated GOx@ZIF-8 crystals that underwent different crystallization pathways with atomic-scale resolution.[25] These investigations into protein@MOF crystallization pathways and outcomes led to detailed correlations between synthetic conditions and properties. However, our limited understanding of the precise spatial localization and distribution patterns of proteins embedded with the MOF crystals challenges our ability to control crystallization pathways and protein properties predictively. To address this challenge, we leveraged the intrinsic iron oxide mineral core within Fn as a contrast agent to directly visualize individual Fn proteins using electron microscopy methods. It is important to note that proteins with different properties than Fn may influence alternative MOF crystallization pathways and protein spatial distributions. However, due to the number of parameters that may be adjusted to form protein@MOF crystals (ligand-to-metal ratio, protein surface charge, precursor concentrations, addition of chemical additives, or post-synthetic workup procedure), we believe that Fn serves as a functional system to explore how these conditions can control protein spatial localization and distribution patterns. Further, this is key for understanding generalizable crystallization mechanisms and developing models that can predict the formation mechanisms and properties of new protein@MOF biocomposites.

The SEM analysis on the Fn@MOFs provided direct evidence of surface-bound proteins. We utilized this direct protein core visualization to investigate the impact of post-synthetic SDS surfactant washing. Our findings indicated that the commonly employed surfactant wash removed surface-adsorbed protein, albeit with significant MOF support degradation and partial removal of proteins encapsulated near the surface of the MOF crystals. This is important to highlight,

as it can lead to inaccurate assessments of the encapsulation efficiencies and activities in protein@MOFs.[7,21,42,45] These results indicate that significant optimization must be performed to remove surface-adsorbed protein without removing surface-localized protein and degrading the MOF support.

We next analyzed the Fn@MOFs using TEM and observed significant protein spatial distribution variations for the crystals formed. TEM analysis of the Fn@ZIF-based biocomposites revealed that lower ligand-to-metal ratios produce $Zn(mIm)_2$ crystalline material phases (e.g., Fn@dia(Zn) and Fn@ZIF-C) with spatially uniform protein densities compared to the higher ratios, which resulted in Fn@ZIF-8 crystals with surface-localized protein. Using controlled-dose dry-cryoET, we obtained a direct 3D visualization of protein@MOFs with individual protein resolution. Our ET quantification revealed that most proteins embedded into the ZIF-8 crystal are partially exposed on the crystal surface. This supports previous work from Pan *et al.,* who proposed partially exposed surface protein encapsulation from site-directed spin labeling combined with electron paramagnetic spectroscopy data for lysozyme@ZIF-8 crystals.[59] Additionally, previous studies on enzyme@ZIF-8 crystals have reported activity in cases where the MOF pore apertures are too narrow to enable substrate access.[23,60,61] Recently, Tong *et al*. attributed this activity to amorphous phases and coordination defects throughout the ZIF-8 crystal, allowing for larger pores for the substrates to access.[25] Our dry-cryoET analysis suggests that partially exposed surface encapsulated protein may also add to the enabled catalytic activity previously observed if the enzyme active site is partially or fully exposed on the MOF crystal surfaces.

Cross-sections obtained by ET revealed the existence of Fn protein aggregates that span the surface of the ZIF-8 crystals, regardless of whether the crystals were formed under low or high protein concentrations. We quantified higher clustering or greater extents of protein aggregation in the Fn@ZIF-8 crystal formed at lower protein concentrations and more homogenous aggregation in the crystal formed at higher protein concentrations. Understanding protein aggregation is vital, as it can impact protein stability and catalytic activity through limitations in substrate mass transfer, spatial confinement, and denaturation from protein-protein interactions due to encapsulation.[19,62,63] Therefore, the ability to directly resolve individual proteins and quantify protein aggregation in protein@MOFs is paramount for characterizing, quantifying, and mitigating these effects. Additionally, the ET cross-sections of the Fn@ZIF-8 crystal formed at high Fn concentrations showed significant macroporous areas with diminished Fn density. This contradicts previous hypotheses that protein aggregation causes rough MOF surfaces and hierarchical pore formation.[17] We previously attributed this macropore formation to possible aggregation and crystallization of irregular amorphous phases.[28] However, the smooth pore surfaces and lack of Fn indicate alternative crystallization mechanisms. These collective insights gained by ET studies and quantification are fundamental to our future understanding of how proteins control and influence the crystallization pathways of MOFs.

The ferritin superfamily is a class of iron storage proteins that can incorporate up to ~4500 Fe atoms inside their hollow protein nanocavities.[64]

4. Conclusion

This methodology demonstrates that using horse spleen Fn as a representative protein for encapsulation into MOFs allowed us to achieve individual protein core resolution in our SEM, TEM, and ET analysis. With direct visualization of the Fn protein cores, we were able to develop holistic 2D and 3D interpretations and quantification of where the proteins spatially lie in the MOF crystals. This work highlights the fundamental connection between protein spatial localization and aggregation and the ZIF-based material phases formed under various synthetic conditions (e.g., ligand-to-metal ratio and protein concentration). These results provide essential insights for future research that relies on a complete structural understanding of protein@MOF biocomposites and aims toward understanding protein spatial location and aggregation during the assembly mechanisms of protein@MOF crystals. Our methodology offers a simple approach for efficient advancements in developing protein-based biohybrid materials. Notably, the Fn protein scaffold is highly amenable to genetic and chemical modification, enabling investigations into how protein-MOF interfaces can be tuned to elucidate how these factors influence protein spatial location, distribution, and aggregation. The methodology presented here can be applied more broadly to other protein immobilization approaches.

5. Methods Section

Materials

All chemicals and reagents were purchased from commercial sources and used without further purification. Ferritin (Fn, Equine Spleen) apoferritin (aFn, Equine Spleen), zinc acetate dihydrate ($Zn(OAc)_2{\cdot}2H_2O$, ≥98%), 2-methylimidazole

(HmIm, 99%), terephthalic acid (98%), sodium dodecyl sulfate (SDS, ≥99%), were purchased from Sigma-Aldrich. The Coomassie Plus (Bradford) assay reagent, 96-well plates, and europium chloride hexahydrate ($EuCl_3.6H_2O$, 99%) were purchased from Fischer Scientific/Pierce. Ultrapure water was used as the solvent for all aqueous solutions and was obtained through a Millipore Milli-Q water purification system (ρ > 18 MΩ cm).

Synthesis of Fn@ZIF-Based Biocomposites and aFn@ZIF-8

In a typical synthesis, 0.5 mL of an aqueous solution with a given protein concentration (0.5 mg/mL or 2.5 mg/mL) was added into a 0.5 mL aqueous solution of a given concentration of HmIm (120 mM, 400 mM, 700 mM, 1400 mM, 2800 mM), and vortexed for 10 s. A 1.0 mL aqueous solution of $Zn(OAc)_2{\cdot}2H_2O$ (40 mM) was added to the combined protein and HmIm solution, then the overall mixture was vortexed for 10 s and aged under static conditions for 22 h at room temperature. The resulting precipitate was recovered by centrifugation at 10,000 rpm for 10 min and subjected to centrifugation-wash cycles three times using Milli-Q water. For SDS-washed biocomposites, the purified ZIF-8 or Fn@ZIF-8 samples (i.e., washed with water 3x) were immersed into a 10% w/w SDS solution (2 mL) for 15 min to remove the surface-adsorbed protein. The resulting solids were recovered by centrifugation, then subjected to centrifuge-wash cycles with water (2 mL, 3x) and ethanol (2 mL, 3x) to remove residual surfactant.

Characterization

Dry-Cryogenic Transmission Electron Microscopy (Dry-CryoTEM)

Lacey carbon grids were purchased from Electron Microscopy Sciences and used as received. Grids were glow discharged for 75 s to increase hydrophilicity before sample preparation. Vitrification was conducted using an Automatic Plunge Freezer ME GP2 (Leica Microsystems). Grid preparation was performed by applying 3 μL of the sample at ambient humidity, and the grids were blotted for 6 s prior to plunging into liquid propane. The dry-cryogenic conditions allow for minimized beam damage, and the low humidity and long blotting time remove the water layers from around the MOFs, resulting in better signal-to-noise images than conventional solvated cryoTEM.[54,55] Dry-cryoTEM samples were placed into a Gatan cryoTEM holder and imaged on a JEOL 2100F TEM using a Schottky-type field emission gun operating at 200 kV. Images were recorded using Serial EM software and a Gatan OneView CMOS camera at 4k × 4k resolution.

Dry-State Cryogenic Electron Tomography (Dry-CryoET)

The dry-cryoET samples of the Fn@ZIF-8 crystals were prepared by following the procedure for dry-cryoTEM with one addition: lacey carbon grids were first dry-loaded with 1 μL of 15 nm gold fiducial marker solution. The tomographic tilt series were acquired between ±65° using 2° increments. The acquisition was conducted at a magnification of 30,000× using Serial EM software at a defocus value of -3 μm. During the tilt series acquisition, an electron flux of 1.09 $e^{-}{\cdot}Å^{-2}{\cdot}s^{-1}$ was applied with an exposure time of 0.3 s/frame, resulting in a cumulative dosage of ~42.8 $e^{-}{\cdot}Å^{-2}$. Before the dry-cryoET experiments, a dose series was acquired up to ~82.5 $e^{-}Å^{-2}$, showing no significant beam damage on the Fn@ZIF-8 crystals or Fn cores under such a cumulative dose. The tilt series were aligned based on the automated tracking of 15 nm gold fiducial markers,[65] and the reconstruction was conducted with IMOD software using SIRT with 5 iterations.[66] The reconstructed data was manually segmented using IMOD[67] and visualized using UCSF Chimera[68] software.

Scanning Electron Microscopy (SEM)

Scanning electron microscopy images were acquired using an FEI Magellan 400 XHR system. Energy dispersive spectroscopic (EDS) images were obtained using the same SEM system with an equipped EDS detector (Oxford Instruments, 80 mm^2, with Aztec software). Before SEM imaging, samples were drop-cast on an aluminum stub using conductive carbon tape and sputter-coated with ~4 nm iridium (Quorum Q150T) to prevent charging.

Powder X-ray Diffraction (PXRD)

PXRD patterns were acquired using a Rigaku SmartLab X-ray diffractometer utilizing X-rays generated at 40 kV and 44 mA with Cu Kα irradiation (λ = 1.5418 Å) while in Bragg–Brentano mode using zero background plates. Results were plotted with background subtraction using IGOR software.

Fourier Transform Infrared (FTIR) Spectroscopy

FTIR spectroscopy was conducted on the Jasco FT/IR-4700 spectrophotometer equipped with the ATR monolithic diamond sampling stage. The FTIR spectra were recorded in the 4000–400 cm^{-1} spectral range using 128 scans at a spectral resolution of 4 cm^{-1}. Samples prepared for FTIR analysis were prepared by following the procedure for synthesizing the Fn@ZIF-based biocomposites with the following modification. After immersion into the SDS solution, the resulting solids were recovered by centrifugation, then subjected to centrifuge-wash cycles with water (2 mL, 6x) to remove residual surfactant and avoid phase transitions that would result from washing with ethanol.[42]

Protein Encapsulation Efficiency Determination

The linearized Bradford method[46] was used to assess the concentration differences of proteins in the supernatant before and after encapsulation to evaluate the amount of loaded protein within the biocomposites. The estimated percent encapsulation efficiency (EE%) was averaged across ten independent analyses. Briefly, 20 μL of the sample was added to a 96-well plate, followed by 200 μL of 2.5-fold diluted Coomassie Assay Reagent. The mixed solution was incubated for 5 min, and then the absorbance of the solution was measured at 450 nm and 590 nm using a UV-vis spectrophotometer. The concentration of the proteins in the supernatants is proportional to the absorption strength at 590 nm divided by the absorption strength at 450 nm.[46]

Protein Release Profiles

The Fn release experiments were performed following a modified cumulative release method.[42] The Fn release profiles were conducted on the Fn@ZIF-8 (70:1, 35:1, and 17.5:1), 10:1 Fn@dia(Zn), and 4:1 Fn@ZIF-C biocomposites formed at protein concentrations of 0.5 mg/mL. Briefly, 2.0 mg of the obtained ZIF-based biocomposites were dispersed in citric acid buffer solution (1.0 mL, 100 mM, pH 5.5) and vortexed for 3 s. After specific times of incubation, the solutions were vortexed for 3 s and then centrifuged at 10,000 rpm for 1 min. Then, 20 μL of the supernatant was added to a 96-well plate and replaced with an equal amount of the citrate acid buffer solution. Afterwards, 200 μL of 2.5-fold diluted Coomassie Assay Reagent was added to the 20 uL of supernatant. The mixed solution was incubated for 5 min, and then the absorbance of the solution was measured at 450 nm and 590 nm using a UV-vis spectrophotometer. The concentration of the proteins in the supernatants is proportional to the absorption strength at 590 nm divided by the absorption strength at 450 nm.[46] The cumulative release profiles were calculated as a function of time and were repeated 10 times.

Statistical Analysis

The spatial distribution analysis of the Fn cores in the dry-cryoET reconstructions was performed using in-house Matlab scripts. Analysis was performed on the position of the Fn cores in the two dry-cryoET reconstructions for the Fn@ZIF-8 crystals. The 70:1 Fn@ZIF-8 (0.5 mg/mL) reconstruction (**Figure 8a**) contained 1573 segmented Fn particles, and the 70:1 Fn@ZIF-8 (2.5 mg/mL) reconstruction (**Figure 8c**) contained 843 segmented Fn particles. The Fn particles were labeled using distance-to-surface analysis and clustering analysis (full details in SI). The results are expressed as percentages in **Figure 10** with absolute numbers available in **Figure S17** and **Figure S19**.

Supporting Information

Supporting Information is available from the Wiley Online Library or the author.

Acknowledgments

This work was supported by the National Science Foundation CBET Award #2102033. The authors acknowledge the use of facilities and instrumentation at the UC Irvine Materials Research Institute (IMRI), which was supported in part by the National Science Foundation through the UC Irvine Materials Research Science and Engineering Center (DMR-2011967). Use of the Stanford Synchrotron Radiation Lightsource, SLAC National Accelerator Laboratory, is supported by the U.S. Department of Energy, Office of Science, Office of Basic Energy Sciences under Contract No. DE-AC02-76SF00515. In addition, R. D. was supported by a National Science Foundation Graduate Research Fellowship, and S.L.C. was supported by the University of California's Leadership Excellence through Advanced Degrees (UC LEADS) Program.

Conflict of Interest

The authors declare no competing financial interest.

Data Availability Statement

The data that support the findings of this study are available from the corresponding author upon reasonable request.

References

[1] L. M. Ellerby, C. R. Nishida, F. Nishida, S. A. Yamanaka, B. Dunn, J. S. Valentine, J. I. Zink, *Science* **1992**, *255*, 1113.

[2] G. F. Bickerstaff, In *Immobilization of Enzymes and Cells* (Ed.: Bickerstaff, G. F.), Humana Press, Totowa, NJ, **1997**, pp. 1–11.

[3] C. Lei, Y. Shin, J. Liu, E. J. Ackerman, *J. Am. Chem. Soc.* **2002**, *124*, 11242.

[4] D. M. Vriezema, M. Comellas Aragonès, J. A. A. W. Elemans, J. J. L. M. Cornelissen, A. E. Rowan, R. J. M. Nolte, *Chem. Rev.* **2005**, *105*, 1445.

[5] M. Yan, J. Ge, Z. Liu, P. Ouyang, *J. Am. Chem. Soc.* **2006**, *128*, 11008.

[6] D. Fujita, K. Suzuki, S. Sato, M. Yagi-Utsumi, Y. Yamaguchi, N. Mizuno, T. Kumasaka, M. Takata, M. Noda, S. Uchiyama, K. Kato, M. Fujita, *Nat. Commun.* **2012**, *3*, 1093.

[7] K. Liang, R. Ricco, C. M. Doherty, M. J. Styles, S. Bell, N. Kirby, S. Mudie, D. Haylock, A. J. Hill, C. J. Doonan, P. Falcaro, *Nat. Commun.* **2015**, *6*, 7240.

[8] C. Doonan, R. Riccò, K. Liang, D. Bradshaw, P. Falcaro, *Acc. Chem. Res.* **2017**, *50*, 1423.

[9] G. Férey, *Chem. Soc. Rev.* **2007**, *37*, 191.

[10] Functional Porous Coordination Polymers - Kitagawa - 2004 - Angewandte Chemie International Edition - Wiley Online Library, .

[11] Introduction to Metal–Organic Frameworks, *Chem. Rev.* **2012**, *112*, 673.

[12] W. Liang, P. Wied, F. Carraro, C. J. Sumby, B. Nidetzky, C.-K. Tsung, P. Falcaro, C. J. Doonan, *Chem. Rev.* **2021**, *121*, 1077.

[13] S. Huang, G. Chen, G. Ouyang, *Chem. Soc. Rev.* **2022**, *51*, 6824.

[14] The Chemistry and Applications of Metal-Organic Frameworks | Science, .

[15] W. Liang, R. Ricco, N. K. Maddigan, R. P. Dickinson, H. Xu, Q. Li, C. J. Sumby, S. G. Bell, P. Falcaro, C. J. Doonan, *Chem. Mater.* **2018**, *30*, 1069.

[16] H. Xia, N. Li, X. Zhong, Y. Jiang, *Front. Bioeng. Biotechnol.* **2020**, *8*.

[17] F. Lyu, Y. Zhang, R. N. Zare, J. Ge, Z. Liu, *Nano Lett.* **2014**, *14*, 5761.

[18] N. K. Maddigan, O. M. Linder-Patton, P. Falcaro, C. J. Sumby, S. G. Bell, C. J. Doonan, *ACS Appl. Mater. Interfaces* **2021**, *13*, 51867.

[19] F.-K. Shieh, S.-C. Wang, C.-I. Yen, C.-C. Wu, S. Dutta, L.-Y. Chou, J. V. Morabito, P. Hu, M.-H. Hsu, K. C.-W. Wu, C.-K. Tsung, *J. Am. Chem. Soc.* **2015**, *137*, 4276.

[20] W.-H. Chen, M. Vázquez-González, A. Zoabi, R. Abu-Reziq, I. Willner, *Nat. Catal.* **2018**, *1*, 689.

[21] W. Liang, H. Xu, F. Carraro, N. K. Maddigan, Q. Li, S. G. Bell, D. M. Huang, A. Tarzia, M. B. Solomon, H. Amenitsch, L. Vaccari, C. J. Sumby, P. Falcaro, C. J. Doonan, *J. Am. Chem. Soc.* **2019**, *141*, 2348.

[22] X. Wu, H. Yue, Y. Zhang, X. Gao, X. Li, L. Wang, Y. Cao, M. Hou, H. An, L. Zhang, S. Li, J. Ma, H. Lin, Y. Fu, H. Gu, W. Lou, W. Wei, R. N. Zare, J. Ge, *Nat. Commun.* **2019**, *10*, 5165.

[23] G. Chen, X. Kou, S. Huang, L. Tong, Y. Shen, W. Zhu, F. Zhu, G. Ouyang, *Angew. Chem. Int. Ed.* **2020**, *59*, 2867.

[24] L. Wang, P. Sun, Y. Yang, H. Qiao, H. Tian, D. Wu, S. Yang, Q. Yuan, J. Wang, *Nanomaterials* **2021**, *11*, 2171.

[25] L. Tong, S. Huang, Y. Shen, S. Liu, X. Ma, F. Zhu, G. Chen, G. Ouyang, *Nat. Commun.* **2022**, *13*, 951.

[26] B. P. Carpenter, A. R. Talosig, J. T. Mulvey, J. G. Merham, J. Esquivel, B. Rose, A. F. Ogata, D. A. Fishman, J. P. Patterson, *Chem. Mater.* **2022**, *34*, 8336.

[27] X. Gong, K. Gnanasekaran, Z. Chen, L. Robison, M. C. Wasson, K. C. Bentz, S. M. Cohen, O. K. Farha, N. C. Gianneschi, *J. Am. Chem. Soc.* **2020**, *142*, 17224.

[28] A. F. Ogata, A. M. Rakowski, B. P. Carpenter, D. A. Fishman, J. G. Merham, P. J. Hurst, J. P. Patterson, *J. Am. Chem. Soc.* **2020**, *142*, 1433.

[29] D. Feng, T.-F. Liu, J. Su, M. Bosch, Z. Wei, W. Wan, D. Yuan, Y.-P. Chen, X. Wang, K. Wang, X. Lian, Z.-Y. Gu, J. Park, X. Zou, H.-C. Zhou, *Nat. Commun.* **2015**, *6*, 5979.

[30] J. Guo, L. Yang, Z. Gao, C. Zhao, Y. Mei, Y.-Y. Song, *ACS Catal.* **2020**, *10*, 5949.

[31] J. Liang, M. Y. Bin Zulkifli, J. Yong, Z. Du, Z. Ao, A. Rawal, J. A. Scott, J. R. Harmer, J. Wang, K. Liang, *J. Am. Chem. Soc.* **2022**, *144*, 17865.

[32] J. Liang, B. Johannessen, Z. Wu, R. F. Webster, J. Yong, M. Y. B. Zulkifli, J. S. Harbort, Y. R. Cheok, H. Wen, Z. Ao, B. Kong, S. L. Y. Chang, J. Scott, K. Liang, *Adv. Mater.* **2022**, *34*, 2205674.
[33] T. Man, C. Xu, X.-Y. Liu, D. Li, C.-K. Tsung, H. Pei, Y. Wan, L. Li, *Nat. Commun.* **2022**, *13*, 305.
[34] W. H. Massover, *Micron* **1993**, *24*, 389.
[35] N. R. Wilson, P. A. Pandey, R. Beanland, R. J. Young, I. A. Kinloch, L. Gong, Z. Liu, K. Suenaga, J. P. Rourke, S. J. York, J. Sloan, *ACS Nano* **2009**, *3*, 2547.
[36] T.-T. Chen, J.-T. Yi, Y.-Y. Zhao, X. Chu, *J. Am. Chem. Soc.* **2018**, *140*, 9912.
[37] W. Huang, H. Yuan, H. Yang, X. Ma, S. Huang, H. Zhang, S. Huang, G. Chen, G. Ouyang, *Nat. Commun.* **2023**, *14*, 3644.
[38] G. Chen, S. Huang, Y. Shen, X. Kou, X. Ma, S. Huang, Q. Tong, K. Ma, W. Chen, P. Wang, J. Shen, F. Zhu, G. Ouyang, *Chem* **2021**, *7*, 2722.
[39] G. Jutz, P. van Rijn, B. Santos Miranda, A. Böker, *Chem. Rev.* **2015**, *115*, 1653.
[40] R. Banerjee, A. Phan, B. Wang, C. Knobler, H. Furukawa, M. O'Keeffe, O. M. Yaghi, *Science* **2008**, *319*, 939.
[41] S. Li, M. Dharmarwardana, R. P. Welch, C. E. Benjamin, A. M. Shamir, S. O. Nielsen, J. J. Gassensmith, *ACS Appl. Mater. Interfaces* **2018**, *10*, 18161.
[42] F. Carraro, M. de J. Velásquez-Hernández, E. Astria, W. Liang, L. Twight, C. Parise, M. Ge, Z. Huang, R. Ricco, X. Zou, L. Villanova, C. O. Kappe, C. Doonan, P. Falcaro, *Chem. Sci.* **2020**, *11*, 3397.
[43] M. Ge, Y. Wang, F. Carraro, W. Liang, M. Roostaeinia, S. Siahrostami, D. M. Proserpio, C. Doonan, P. Falcaro, H. Zheng, X. Zou, Z. Huang, *Angew. Chem. Int. Ed.* **2021**, *60*, 11391.
[44] C. Daiguebonne, N. Kerbellec, O. Guillou, J.-C. Bünzli, F. Gumy, L. Catala, T. Mallah, N. Audebrand, Y. Gérault, K. Bernot, G. Calvez, *Inorg. Chem.* **2008**, *47*, 3700.
[45] I. Amenabar, S. Poly, W. Nuansing, E. H. Hubrich, A. A. Govyadinov, F. Huth, R. Krutokhvostov, L. Zhang, M. Knez, J. Heberle, A. M. Bittner, R. Hillenbrand, *Nat. Commun.* **2013**, *4*, 2890.
[46] T. Zor, Z. Selinger, *Anal. Biochem.* **1996**, *236*, 302.
[47] J. Cases Díaz, B. Lozano-Torres, M. Giménez-Marqués, *Chem. Mater.* **2022**, *34*, 7817.
[48] C. Wiktor, S. Turner, D. Zacher, R. A. Fischer, G. V. Tendeloo, *Microporous Mesoporous Mater.* **2012**, *162*, 131.
[49] J. P. Patterson, P. Abellan, M. S. Jr. Denny, C. Park, N. D. Browning, S. M. Cohen, J. E. Evans, N. C. Gianneschi, *J. Am. Chem. Soc.* **2015**, *137*, 7322.
[50] Y. Zhu, J. Ciston, B. Zheng, X. Miao, C. Czarnik, Y. Pan, R. Sougrat, Z. Lai, C.-E. Hsiung, K. Yao, I. Pinnau, M. Pan, Y. Han, *Nat. Mater.* **2017**, *16*, 532.
[51] D. Zhang, Y. Zhu, L. Liu, X. Ying, C.-E. Hsiung, R. Sougrat, K. Li, Y. Han, *Science* **2018**, *359*, 675.
[52] Y. Li, K. Wang, W. Zhou, Y. Li, R. Vila, W. Huang, H. Wang, G. Chen, G.-H. Wu, Y. Tsao, H. Wang, R. Sinclair, W. Chiu, Y. Cui, *Matter* **2019**, *1*, 428.
[53] L. Liu, D. Zhang, Y. Zhu, Y. Han, *Commun. Chem.* **2020**, *3*, 1.
[54] P. J. Hurst, A. A. Graham, J. P. Patterson, *ACS Polym. Au* **2022**, *2*, 501.
[55] A. Rizvi, J. T. Mulvey, B. P. Carpenter, R. Talosig, J. P. Patterson, *Chem. Rev.* **2021**, *121*, 14232.
[56] Self-Assembly of Extracellular Vesicle-like Metal–Organic Framework Nanoparticles for Protection and Intracellular Delivery of Biofunctional Proteins | Journal of the American Chemical Society, .
[57] R. f. Egerton, *Microsc. Res. Tech.* **2012**, *75*, 1550.
[58] B. P. Carpenter, A. Rain Talosig, B. Rose, G. D. Palma, J. P. Patterson, *Chem. Soc. Rev.* **2023**.
[59] Y. Pan, H. Li, J. Farmakes, F. Xiao, B. Chen, S. Ma, Z. Yang, *J. Am. Chem. Soc.* **2018**, *140*, 16032.
[60] X. Wu, H. Yue, Y. Zhang, X. Gao, X. Li, L. Wang, Y. Cao, M. Hou, H. An, L. Zhang, S. Li, J. Ma, H. Lin, Y. Fu, H. Gu, W. Lou, W. Wei, R. N. Zare, J. Ge, *Nat. Commun.* **2019**, *10*, 5165.
[61] S.-Y. Chen, W.-S. Lo, Y.-D. Huang, X. Si, F.-S. Liao, S.-W. Lin, B. P. Williams, T.-Q. Sun, H.-W. Lin, Y. An, T. Sun, Y. Ma, H.-C. Yang, L.-Y. Chou, F.-K. Shieh, C.-K. Tsung, *Nano Lett.* **2020**, *20*, 6630.
[62] Z. Zhong, S. Pang, Y. Wu, S. Jiang, J. Ouyang, *J. Chem. Technol. Biotechnol.* **2017**, *92*, 1841.
[63] Q. Liu, J. Chapman, A. Huang, K. C. Williams, A. Wagner, N. Garapati, K. A. Sierros, C. Z. Dinu, *ACS Appl. Mater. Interfaces* **2018**, *10*, 41326.

[64] A. Yévenes, In *Macromolecular Protein Complexes: Structure and Function* (Eds.: Harris, J. R.; Marles-Wright, J.), Springer International Publishing, Cham, **2017**, pp. 75–102.
[65] M. Radermacher, In *Electron Tomography: Methods for Three-Dimensional Visualization of Structures in the Cell* (Ed.: Frank, J.), Springer, New York, NY, **2006**, pp. 245–273.
[66] J. R. Kremer, D. N. Mastronarde, J. R. McIntosh, *J. Struct. Biol.* **1996**, *116*, 71.
[67] K. K. K. Mai, B.-H. Kang, In *Plant Protein Secretion: Methods and Protocols* (Ed.: Jiang, L.), Springer, New York, NY, **2017**, pp. 97–104.
[68] E. F. Pettersen, T. D. Goddard, C. C. Huang, G. S. Couch, D. M. Greenblatt, E. C. Meng, T. E. Ferrin, *J. Comput. Chem.* **2004**, *25*, 1605.